Oceanologia, corrected, in press
Polish Academy of Sciences
Institute of Oceanology
Open access article under the CC BY license
https://doi.org/10.5697/GCMF7307

Tidal, wind and density influences on the circulation of the Gulf of Oman

Ali Khosh Kholgh*, Mohammad Hossein Kazeminezhad, Majid Noranian Esfahani

Abstract
The relative contributions of tidal, wind, and density forcing to the general circulation of the Gulf of Oman are investigated using a high-resolution three-dimensional hydrodynamic model. Currents were simulated for the year 2012 under spatially and temporally varying boundary conditions, including tidal elevation, atmospheric forcing, and density stratification derived from TPXO8, ERA5, and HYCOM datasets, respectively.
Results reveal a seasonally reversing circulation system characterized by subtropical gyres with positive vorticity during the cold season and negative vorticity during the warm season. Maximum current velocities reach approximately 0.5 m s^{-1} under tidal forcing and increase to about 0.6 m s^{-1} when wind effects are included.
Analysis of depth-averaged kinetic energy indicates that tidal forcing establishes the dominant energetic framework of the basin. Wind forcing contributes approximately 2.50% to the basin-scale kinetic energy, primarily during the Southwest monsoon, while density-driven processes account for about 2.18%, with a more pronounced influence during winter conditions. Although density effects do not significantly improve statistical model performance metrics, they play an important role in shaping vertical stratification and subsurface circulation.
Overall, the results highlight a tide-dominated system in which wind modulates seasonal variability and density forcing contributes to vertical structure and basin-scale energetics.

Keywords
Mike3D; Ocean circulation; Regional ocean modeling; Kinetic energy

Iranian National Institute for Oceanography and Atmospheric Science (INIOAS), Tehran, 1411813389, Iran
***Correspondence**: a_khosh@inio.ac.ir (A. Khosh Kholgh)

Received: 23 February 2026; **revised:** 10 August 2026; **accepted**: 26 October 2026

1. Introduction

Understanding shelf circulation is essential for marine structure design, offshore engineering applications, environmental management, and coastal development planning. In marginal seas influenced by multiple forcing mechanisms, the interaction between tidal currents, wind stress, and density-driven processes governs hydrodynamic variability and energy distribution. Quantifying the relative contribution of these forcing mechanisms remains a fundamental issue in physical oceanography, particularly in semi-enclosed basins where tidal exchange and monsoon forcing coexist (Reynolds, 1993; Simpson and Sharples, 2012).

The Gulf of Oman is a strategically important basin connecting the Strait of Hormuz to the Arabian Sea. It extends between 56.32°E and 61.75°E and 22.35°N and 25.81°N, bordered by Iran and Pakistan to the north and Oman to the south (Figure 1). The basin narrows toward the Strait of Hormuz and reaches depths of approximately 3400 m in its eastern sector. Although no major permanent rivers discharge into the basin, seasonal freshwater inputs and exchange processes with the Persian Gulf significantly influence its hydrographic structure.

The hydrodynamic regime of the Gulf of Oman is controlled by three primary mechanisms: tidal forcing, monsoon-driven wind stress, and density gradients associated with the exchange between Persian Gulf Water (PGW) and Indian Ocean Surface Water (IOSW). The region experiences strong seasonal variability due to the Northeast (winter) and Southwest (summer) monsoons (Schott and McCreary Jr, 2001; Vinayachandran et al., 2013). During winter, northeasterly winds dominate, while in summer persistent southwesterly winds modify surface circulation and enhance coastal upwelling processes (Wiggert et al., 2005; Resplandy et al., 2011). These seasonal reversals alter circulation patterns, stratification, and energy distribution across the basin.

Previous investigations have described the general circulation of the Gulf of Oman and its exchange processes

© 2026 The Author(s). This is the Open Access article distributed under the terms of the Creative Commons Attribution Licence.

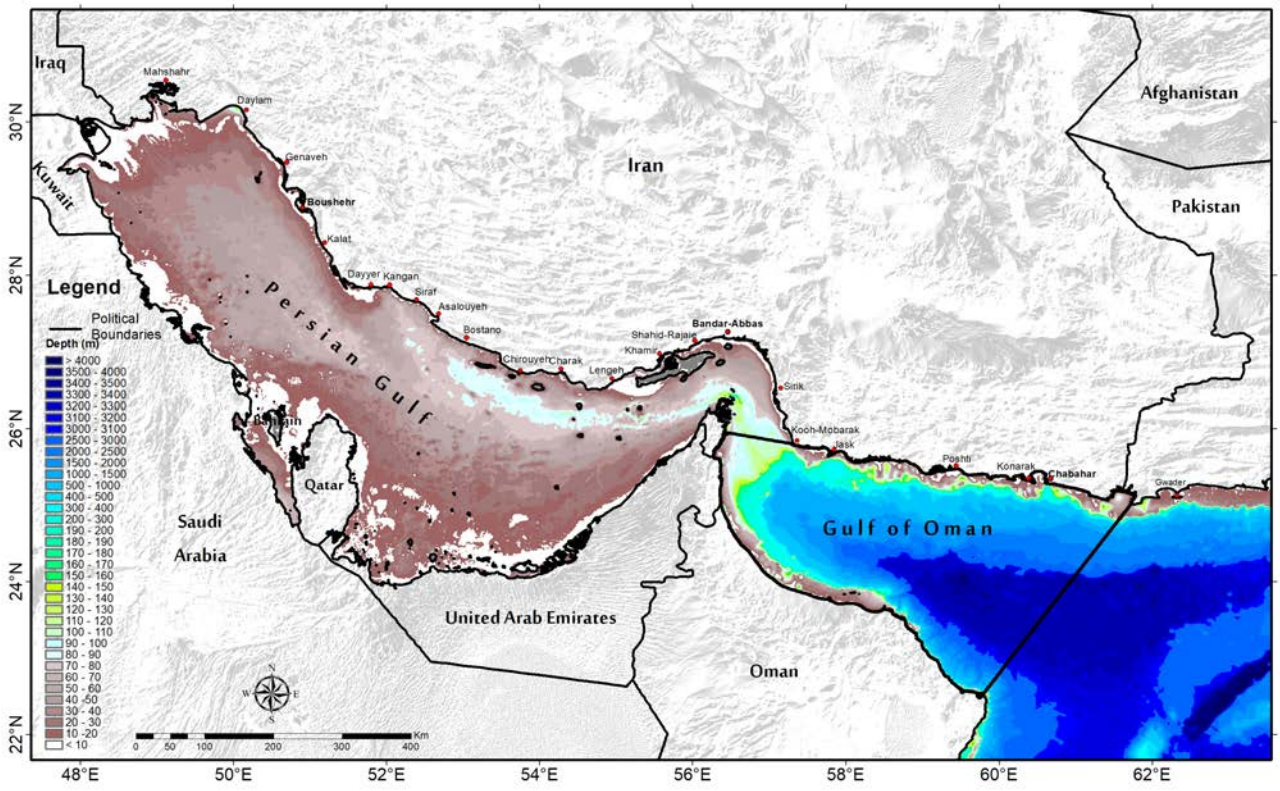


Figure 1. Location and bathymetry of the Gulf of Oman showing the connection between the Persian Gulf and the Arabian Sea. Bathymetric data are derived from GEBCO (2024) and local hydrographic surveys near the Iranian coast.

with the Persian Gulf. Reynolds (1993) identified a double-gyre circulation structure using drifting buoy observations. Pous et al. (2004) examined hydrology and circulation patterns associated with Persian Gulf Water outflow. Ezam et al. (2010) applied three-dimensional numerical modeling to evaluate the spreading and vertical structure of PGW. More recent studies using regional and global ocean models have further improved understanding of seasonal variability and exchange processes in the northern Arabian Sea and adjacent basins (Thoppil and Hogan, 2010; Trott et al., 2017; Deshpande et al., 2021).

Despite these contributions, quantitative assessment of the relative roles of tidal, wind-driven, and density-induced forcing – particularly along the Iranian continental shelf – remains limited. Moreover, few studies have adopted an energy-based framework to explicitly separate and compare the hydrodynamic response under different forcing scenarios in this monsoon-influenced basin. Given ongoing coastal development along the Iranian shoreline and the strategic importance of this region, a detailed and quantitatively constrained hydrodynamic assessment is required.

The objective of the present study is to quantify the relative contribution of tidal, wind, and density- driven processes to shelf circulation in the northern Gulf of Oman using three-dimensional hydrodynamic model (MIKE 3 FM). The year 2012 was selected as the main simulation year based on the availability of complete atmospheric and oceanographic datasets and concurrent in-situ current observations for model validation. A staged modeling framework is adopted to facilitate comparisons among simulations of currents driven by tides, tide–wind interactions, and combined tide–wind–density effects. This framework enables explicit separation of forcing mechanisms and provides a quantitative evaluation of their contribution to circulation patterns and depth-averaged kinetic energy along the Iranian shelf.

The paper is structured as follows. Section 2 describes the datasets and numerical model configuration. Section 3 presents model validation against field measurements. Section 4 analyzes seasonal circulation patterns and the relative contributions of different forcing mechanisms. Section 5 concludes the study and discusses its physical implications.

2. Materials and methods

To simulate hydrodynamic variability in the study area, tidal, atmospheric, and oceanographic datasets were incorporated into a three-dimensional numerical framework. The datasets and numerical model configuration are described in the following subsections.

2.1 Datasets

2.1.1 Bathymetry

Bathymetric data were primarily obtained from the General Bathymetric Chart of the Oceans (GEBCO) dataset, which provides global coverage at a spatial resolution of 30 arc-seconds (approximately 1 km in the study region). The dataset integrates ship-based soundings and satellite-derived depth estimates to produce a consistent gridded representation of seafloor topography (Weatherall et al., 2024).

In nearshore areas along the Iranian coast, higher-resolution local hydrographic survey data were incorporated to improve the representation of coastal bathymetric gradients. These local datasets were combined with the GEBCO bathymetry to improve the representation of shallow regions, where coastal circulation processes and energy estimates are sensitive to bottom topography. Both the local survey and GEBCO bathymetric datasets were referenced to a common vertical datum, namely Mean Sea Level (MSL). In the overlap zones, the local survey data were integrated with the GEBCO bathymetry using nearest-neighbour interpolation, while preserving the higher spatial resolution of the local survey data in the nearshore areas. The consistency of the resulting bathymetry was evaluated by comparing corresponding depth values at co-located points between the two datasets.

Given the spatial scale of the computational domain and the mesh resolution (1–4 km), the combined bathymetric dataset was considered adequate for resolving basin-scale and shelf-scale features. Although small-scale coastal irregularities may not be fully captured, the adopted bathymetric configuration provides a suitable balance between resolution and computational efficiency for regional hydrodynamic simulations.

2.1.2 Tidal forcing

Tidal elevation and depth-averaged velocity at the open boundaries were derived from the TPXO8-atlas global tidal model using the TMD (Tidal Model Driver) package (Padman and Erofeeva, 2005). TPXO8 provides harmonic tidal constituents at approximately 1/30° spatial resolution and incorporates satellite altimetry and in-situ observations through data assimilation. This version was selected due to its improved accuracy and enhanced assimilation framework compared to earlier TPXO releases.

Major tidal constituents were imposed at the model open boundaries to prescribe tidal elevation and barotropic velocity. The extracted boundary conditions correspond to the period 1 April 2010 to 31 May 2010, for which concurrent observed tidal data were available for calibration purposes.

Regional tidal observations from the National Cartography Center (NCC), including the Jask fixed station and Sirik temporary station, were used to ensure consistency between modeled and observed tidal characteristics along the Iranian coast.

2.1.3 Atmospheric forcing

Atmospheric forcing data for 2012 were obtained from the fifth-generation ECMWF reanalysis dataset ERA5 (Hersbach et al., 2020). The dataset has a spatial resolution of 0.25° and hourly temporal resolution. Wind velocity components at 10 m height, sea-level pressure, air temperature, relative humidity, precipitation, and evaporation were used to compute surface wind stress and air–sea heat fluxes.

Winter monsoon occurs from November to April and is associated with northeasterly winds with average speeds of < 5 m s^{-1} (Figure 2, left), summer monsoon of July–September causes energetic and persistent southerly and

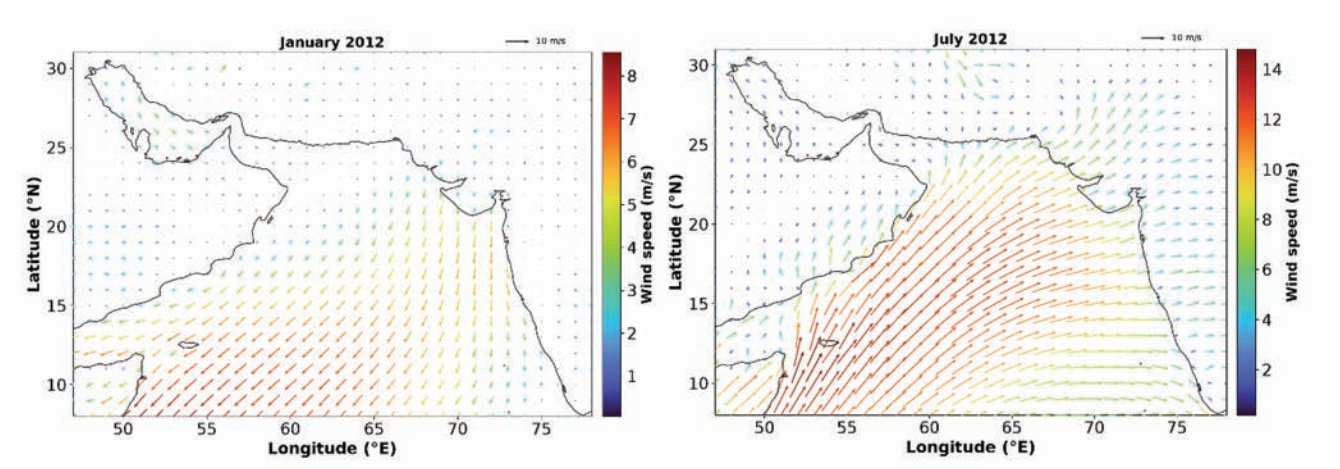


Figure 2. Winds over the Northern Arabian Sea derived from ECMWF ERA5, for January at the NE monsoon season (left), for July at the SW monsoon season (right).

southwesterly winds with average speed of 15 m s^{-1} (Figure 2, right).

This persistent wind regime during summer contributes significantly to ocean circulation and biogeochemical processes in the northern Arabian Sea and the Gulf of Oman. Rest of the months are considered as either post-monsoon (October) or pre-monsoon (May and June) with a transition phase and less persistent wind pattern. Annual wind data analysis of the Gulf of Oman and the northern Arabian Sea shows that predominant wind direction in the Gulf of Oman is westerly to northwesterly, while for the northern Arabian Sea southwesterly is the most frequent wind direction.

Although ERA5 provides high-quality reanalysis data, its spatial resolution may not fully resolve small- scale coastal wind variability influenced by local topography along the Iranian coast. Nevertheless, it is considered appropriate for regional-scale hydrodynamic simulations.

2.1.4 Initial and open boundary conditions

Baroclinic initial and open boundary conditions were derived from the HYCOM global ocean model for the year 2012. The HYCOM dataset provides daily outputs with a horizontal resolution of approximately 1/12° (Metzger et al., 2009).

Temperature, salinity, and three-dimensional velocity fields were extracted to prescribe vertical structure at the open boundaries and to initialize the model domain. These data enable representation of density-driven circulation associated with PGW and IOSW exchange.

2.2 Hydrodynamic model configuration

A three-dimensional hydrodynamic model was implemented using the MIKE 3 FM modeling system. The model solves the three-dimensional incompressible Reynolds-averaged Navier–Stokes (RANS) equations under the Boussinesq and hydrostatic assumptions. The governing equations include continuity, momentum, and scalar transport equations for temperature and salinity. Turbulence effects were represented using the standard k–ε closure scheme, providing estimates of turbulent viscosity and diffusivity. The equations were discretized using a finite volume method on an unstructured mesh, allowing for flexible spatial resolution. An implicit time-stepping scheme was applied to ensure numerical stability, while advection terms were treated using a higher-order upwind scheme to minimize numerical diffusion.

The selection of the MIKE 3 FM modeling system in this study is based on its suitability for simulating hydrodynamic processes in coastal and shelf environments with complex geometries. The flexible unstructured mesh capability of the model allows for variable spatial resolution, enabling higher resolution near the coastline and in dynamically sensitive regions such as the Strait of Hormuz, while maintaining computational efficiency offshore. This feature is particularly advantageous for resolving bathymetric gradients and coastline irregularities in the Gulf of Oman.

In addition, MIKE 3 FM provides a robust three-dimensional baroclinic framework capable of simulating the combined effects of tidal forcing, wind stress, and density gradients within a unified numerical system. The model has been widely applied and validated in coastal and regional hydrodynamic studies, demonstrating reliable performance under mixed forcing conditions. These characteristics make it well suited for the staged modeling approach adopted in this study, where different forcing mechanisms are systematically isolated and compared.Further details of the numerical formulation can be found in the MIKE 3 FM scientific documentation (DHI, 2007).

The computational mesh was generated using an unstructured flexible grid to accurately represent the complex coastline and bathymetry of the Gulf of Oman. To avoid numerical artifacts associated with abrupt resolution changes, particular attention was given to ensuring smooth spatial transitions between regions of different grid resolution. Element sizes vary from approximately 1 km in nearshore and dynamically sensitive areas to about 4 km in offshore regions, with gradual grading applied to minimize sharp gradients in element size.

The hydrodynamic simulations were performed using a finite-volume formulation, which ensures local mass conservation and provides enhanced numerical stability on unstructured meshes. An implicit time- stepping scheme was adopted, allowing stable integration under varying grid resolutions and forcing conditions. The model time step was selected based on the Courant–Friedrichs–Lewy (CFL) condition to ensure numerical stability throughout the domain.

The mesh consisted of 1789 nodes and 3293 triangular elements (Figure 3). Vertically, the water column was discretized using 20 hybrid layers, including 10 sigma layers from the free surface to 50 m depth and 10 fixed z-levels below. This configuration enables accurate representation of both surface processes and deeper baroclinic structure.

In addition, higher-order advection schemes were employed to reduce numerical diffusion and improve the accuracy of momentum and scalar transport. These numerical settings are particularly important in preventing spurious oscillations and grid-induced artifacts in regions with variable resolution.

As shown in Figure 3, measured tidal elevation at Kuhmobarak Harbor (14 April 2010 to 19 May 2010; 30-minute interval) and current velocity measurements obtained using an RCM9 instrument at depths of 25 m, 50 m, and 100 m (3 November 2012 to 30 December 2012), provided by the Iranian National Institute for Oceanography and Atmospheric Science (INIOAS), were used for model validation (see Section 3). For clarity, the two validation sites shown in Figure 3 are hereafter referred to as Station A

In Press

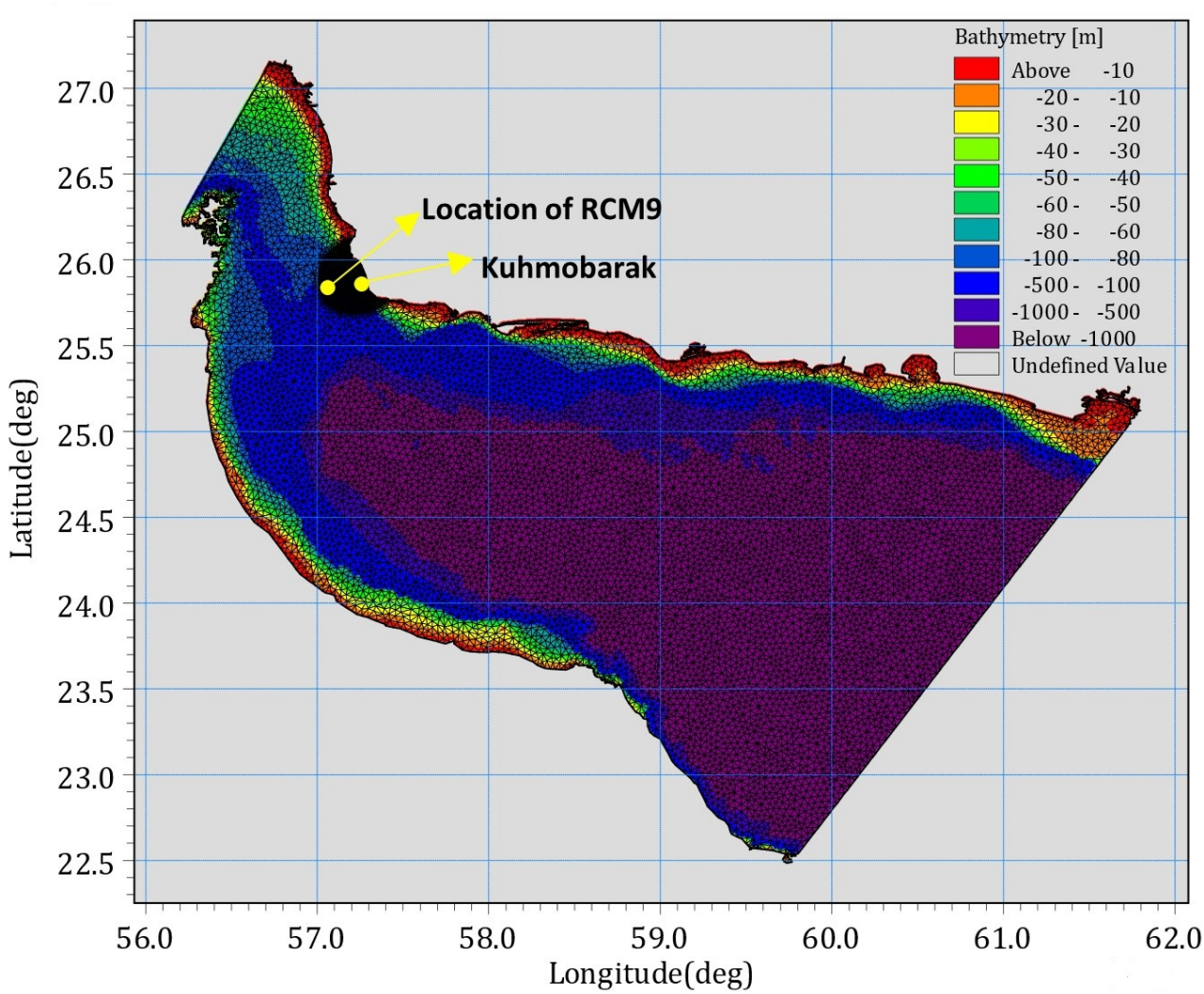


Figure 3. Domain, computational mesh, and bathymetry of the regional hydrodynamic model, along with the locations of observational data used for model calibration and validation.

(the Kuhmobarak tide-gauge site, used for water-level validation) and Station B (the RCM9 mooring site, used for current-velocity validation).

The reliability of the mesh design and numerical configuration is further supported by the model validation results, which demonstrate good agreement between simulated and observed water levels and current velocities across multiple locations and depths. This agreement indicates that the adopted grid structure and numerical schemes do not introduce significant numerical artifacts into the solution.

The nearest open boundary was positioned approximately 100 km from the main area of interest, providing a buffer zone between the boundary and the region where the circulation and exchange processes were investigated. This configuration was selected to minimize the potential influence of the prescribed boundary conditions on the simulated circulation within the area of interest while maintaining a computationally feasible regional model domain. This configuration provides a substantial spatial separation from the main area of interest while allowing the regional circulation and associated exchange processes to be adequately represented.

The wind drag coefficient was used as the calibration parameter. The values presented at Table 1 were selected

Table 1. Selected empirical factors to calculate the wind drag coefficient.

C_a	C_b	W_a	W_b
0.002	0.0055	5 m s^{-1}	8 m s^{-1}

to calculate the wind drag coefficient based on empirical formulae proposed by Wu (1980, 1994) as follow:

$$C_d = \begin{cases} C_a, & W_{10} < W_a, \\ C_a + \dfrac{C_b - C_a}{W_b - W_a}(W_{10} - W_a), & W_a < W_{10} < W_b, \\ C_b, & W_b < W_{10}. \end{cases} \quad (1)$$

where C_a, C_b, W_a and W_b are empirical factors and W_{10} is the wind speed 10 m above the sea surface.

2.3 Simulation scenarios

To isolate the relative contribution of different forcing mechanisms, three numerical experiments were performed within the same staged modeling framework. In the first experiment, only tidal forcing was applied at the open boundaries to simulate purely barotropic tidal circulation. In the second experiment, atmospheric wind stress derived from ERA5 was incorporated in addition to tidal forcing, allowing assessment of the combined effects of tides and wind-driven processes. In the third experiment, baroclinic effects were introduced by including temperature and salinity fields from HYCOM as initial and open boundary conditions, thereby accounting for density-driven circulation associated with water mass exchange.

This staged modeling strategy enables explicit separation of tidal, wind-driven, and density-induced circulation components and facilitates quantitative comparison of their respective contributions to current structure and depth-averaged kinetic energy. Because tidal, wind-driven, and density-induced processes interact nonlinearly (e.g., through tidal straining of density gradients and depth-dependent wind mixing), the staged simulations do not achieve a strict physical separation of independent forcing components. The differences between successive scenarios are therefore interpreted as indicative estimates of the relative importance of each mechanism rather than as exact, additive contributions.

2.4 Model performance evaluation

Model performance was evaluated by comparing simulated and observed water levels and current velocities. The following statistical metrics were used:

The Root Mean Square Error (RMSE) was computed as:

$$RMSE = \sqrt{\frac{1}{N}\sum_{i=1}^{N}(M_i - O_i)^2} \quad (2)$$

The Mean Absolute Error (MAE) was calculated as:

$$MAE = \frac{1}{N}\sum_{i=1}^{N}|M_i - O_i| \quad (3)$$

The Correlation Coefficient (R) was determined as:

$$R = \frac{\sum_{i=1}^{N}(M_i - \overline{M})(O_i - \overline{O})}{\sqrt{\sum_{i=1}^{N}(M_i - \overline{M})^2 \ \sum_{i=1}^{N}(O_i - \overline{O})^2}} \quad (4)$$

The Relative bias normalized by the mean absolute value of the observations:

$$RelBias\% = \frac{\sum_{i=1}^{N}(M_i - O_i)}{\sum_{i=1}^{N}|O_i|} \times 100 \quad (5)$$

where M_i and O_i represent modeled and observed values, respectively, M and O denote their mean values, and N is the number of data points.

3. Model validation and forcing sensitivity

Reliable assessment of model performance is essential prior to analyzing circulation patterns and energy contributions. Due to the availability of field measurements over different time periods, the model was executed for two separate validation intervals. The first simulation covered April–May 2010 to enable validation of tidal water levels against observations at Kuhmobarak Harbor. The second simulation covered November–December 2012 to validate current-velocity profiles using RCM9 measurements at multiple depths. These validation periods were determined by the availability of concurrent, high- frequency in-situ observations rather than by the selection of 2012 as the analysis year. Specifically, the Kuhmobarak tide-gauge record available for tidal validation covers only April–May 2010, whereas the RCM9 current-velocity observations were collected during November–December 2012, directly coinciding with the main simulation year. The use of the 2010 tide-gauge record for tidal validation is justified by the temporal stability of the astronomical tidal constituents represented in TPXO8, which are largely invariant on interannual timescales. Therefore, the 2010 observations provide a suitable independent assessment of the model's tidal performance for the 2012 analysis. In contrast, the current-velocity validation is based directly on observations from 2012, and the full-year production simulation is also conducted for 2012. Consequently, no interannual assumption is required for evaluating the wind- and density-driven components of the circulation.

In Press

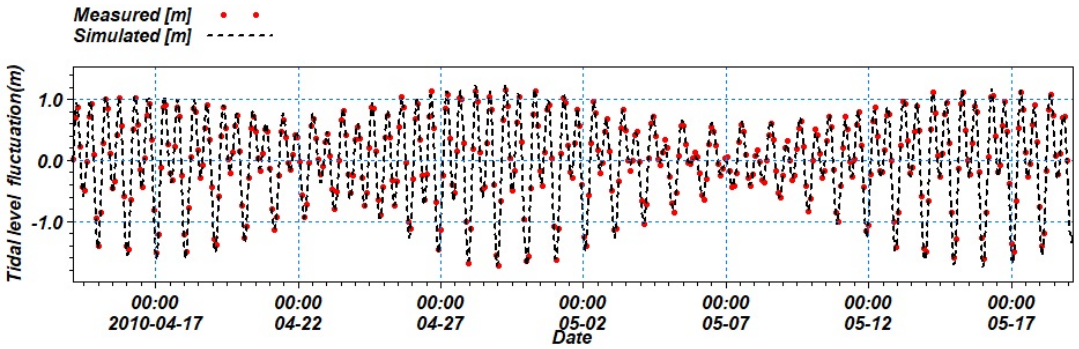


Figure 4. Comparison of simulated and measured tidal level fluctuation at Kuhmobarak.

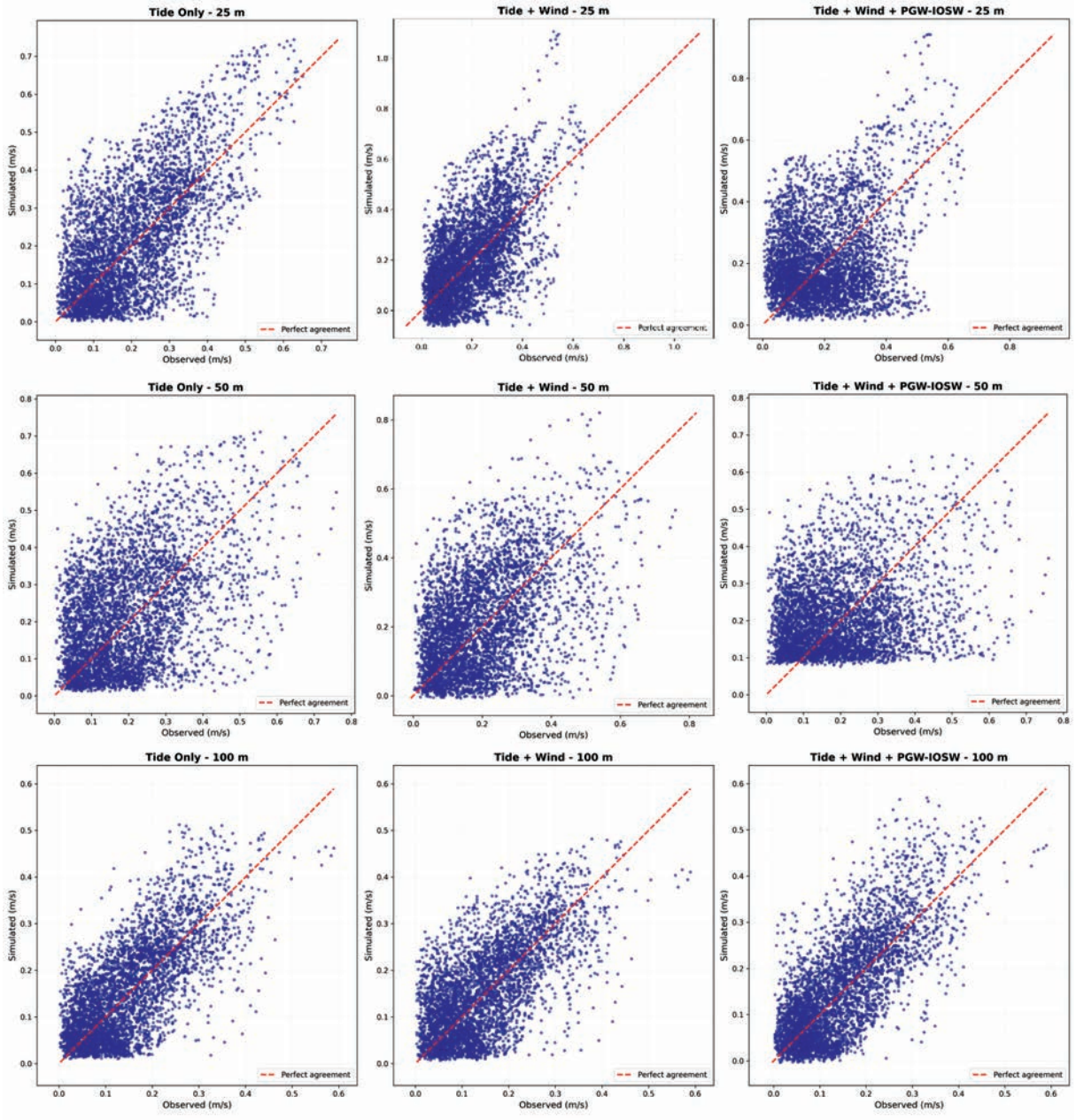


Figure 5. Comparison between simulated and observed current velocities at the surface (25 m), middle (50 m), and bottom (100 m) layers at Station B under three simulation scenarios.

Table 2. Statistical evaluation of simulated versus observed current velocities (mean ± standard deviation) at three depth layers (25 m, 50 m, and 100 m) under different forcing scenarios: tide only, tide–wind, and tide–wind–density (PGW/IOSW exchange), based on RMSE, Bias, MAE, correlation coefficient (R), and relative bias.

Layer	Forcing	RMSE (m s^{-1})	Bias (m s^{-1})	MAE (m s^{-1})	R	RelBias (%)
Surface (25 m)	Tide only	0.16 ± 0.08	0.017 ± 0.005	0.18 ± 0.09	0.58 ± 0.09	8.6 ± 0.89
	Tide + Wind	0.1 ± 0.06	0.016 ± 0.003	0.14 ± 0.08	0.63 ± 0.12	7.5 ± 0.69
	Tide + Wind + PGW/IOSW	0.12 ± 0.07	0.019 ± 0.004	0.15 ± 0.06	0.62 ± 0.13	7.1 ± 0.73
Middle (50 m)	Tide Only	0.14 ± 0.08	0.015 ± 0.007	0.12 ± 0.05	0.65 ± 0.10	8.1 ± 0.92
	Tide + Wind	0.10 ± 0.05	0.014 ± 0.004	0.09 ± 0.04	0.68 ± 0.13	7.3 ± 0.75
	Tide + Wind + PGW/IOSW	0.09 ± 0.05	0.009 ± 0.003	0.08 ± 0.04	0.68 ± 0.12	6.9 ± 0.86
Bottom (100 m)	Tide Only	0.08 ± 0.05	0.014 ± 0.006	0.05 ± 0.02	0.7 ± 0.08	6.8 ± 0.76
	Tide + Wind	0.06 ± 0.04	0.014 ± 0.004	0.04 ± 0.02	0.72 ± 0.09	6.5 ± 0.68
	Tide + Wind + PGW/IOSW	0.05 ± 0.03	0.009 ± 0.002	0.03 ± 0.01	0.71 ± 0.11	6.6 ± 0.71

Following successful validation under these periods, the fully forced configuration (tide + wind + density) was applied for the complete year 2012 to investigate seasonal circulation patterns and quantify forcing contributions. All simulations were conducted using identical grid configuration and numerical parameters to ensure consistency between validation and analysis runs.

Statistical indicators including Root Mean Square Error (RMSE), Mean Absolute Error (MAE), correlation coefficient (R), and Relative bias were used to quantify model accuracy, as defined in Section 2.4.

3.1 Water level (April–May 2010)

Simulated sea surface elevation was compared with observed tidal levels measured at Kuhmobarak Harbor (Station A) between 14 April 2010 and 19 May 2010 at 30-minute intervals. Figure 4 presents the time series comparison between modeled and observed water levels.

Statistical indicators yield an RMSE of 0.08 m, MAE of 0.06 m, correlation coefficient (R) of 0.93, and bias of 0.08 m. In a strongly tide-dominated system such as the Gulf of Oman, a high correlation is expected given the common periodic tidal signal shared by the model and observations, and should not on its own be taken as strong evidence of model skill. The comparable bias and RMSE suggest a mean offset in the model results. After bias correction, the RMSE decreases from 0.08 m to 0.072 m, indicating that the mean offset contributes to the overall error, although most of the remaining error is not explained by this offset alone. Taken together with the correlation coefficient, these metrics indicate that the model with prescribed TPXO8 tidal forcing reproduces the dominant barotropic dynamics reasonably well, while the remaining model–observation differences may arise from other sources of uncertainty.

3.2 Current velocity (November–December 2012)

Model-simulated current velocities were validated against in-situ measurements obtained using an RCM9 current meter deployed at depths of 25 m, 50 m, and 100 m during the period 3 November 2012 to 30 December 2012. Figure 5 shows time series comparisons between simulated and observed velocities at the three depths.

The statistical metrics presented in Table 2 demonstrate a clear improvement in model performance with increasing model complexity and depth. At the surface layer (25 m), the tide-only simulation shows relatively higher errors (RMSE = 0.16 m s^{-1} , MAE = 0.18 m s^{-1}) and lower correlation (R = 0.58), indicating the limited capability of tidal forcing alone in capturing current variability. Incorporating wind forcing reduces both RMSE and MAE (to 0.10 m s^{-1} and 0.14 m s^{-1}, respectively) and improves the correlation (R = 0.63), highlighting the significant contribution of wind- driven processes at the surface. The addition of density-driven exchange (PGW/IOSW) does not lead to a notable improvement and slightly degrades RMSE compared to the tide–wind case.

At the middle layer (50 m), model performance further improves, with lower errors and higher correlations across all scenarios. The tide–wind and tide–wind–density simulations yield similar correlations (R ≈ 0.68), while the latter provides marginal improvements in RMSE and MAE, suggesting a limited but noticeable role of density gradients at this depth.

At the bottom layer (100 m), the model achieves its best performance, with the lowest RMSE (0.05–0.08 m s^{-1}), MAE (0.03–0.05 m s^{-1}), and highest correlation values (R ≈ 0.70–0.72). Differences between forcing scenarios become minimal, indicating that tidal dynamics dominate near-bottom currents, while atmospheric forcing plays a reduced role.

Overall, the relative bias decreases from the surface to the bottom layer and is consistently reduced when wind

In Press

forcing is included, whereas the addition of density effects results in only minor changes. These results suggest that a combined tide–wind forcing is generally sufficient to reproduce current velocities across all depths, with density-driven processes providing only secondary improvements.

Although the inclusion of density-driven processes does not lead to a significant improvement in statistical performance metrics, this does not imply a negligible physical role. Density forcing primarily influences subsurface circulation and vertical stratification, and its contribution is more clearly reflected in basin-scale energetics rather than point-based validation statistics.

It is also noted that the relative bias in Table 2 remains within a comparatively narrow range (~ 6–8%) across all three depth layers and forcing scenarios. The mean bias values are relatively small (0.009–0.019 m s^{-1}) and consistently positive across the different depth layers and forcing scenarios. This consistent positive tendency may indicate a persistent model–observation offset; however, the bias is substantially smaller than the corresponding RMSE values and therefore does not represent the dominant source of the overall error. Thus, this pattern is interpreted cautiously as a possible systematic tendency rather than a confirmed systematic offset.

4. Results

4.1 Seasonal circulation patterns

Based on the validation results presented in Section 3.2, the fully forced configuration was selected to analyze basin-scale seasonal circulation patterns in 2012. In the revised analysis, mesoscale circulation structures, including eddy-like features, are directly examined using MIKE 3 model outputs and subsequently compared with the HYCOM reanalysis dataset. Seasonal mean velocity fields are evaluated at the surface and at depths of 25 m and 60 m during both cold and warm seasons (Figures 6 and 7). Quantitative agreement is assessed at each depth using spatial correlation (R), root-mean-square error (RMSE), and mean bias.

During the winter monsoon (Northeast monsoon), basin-scale circulation is characterized by a two-gyre system, consisting of a cyclonic gyre in the western basin and an anticyclonic gyre in the eastern sector. These coherent rotational structures, clearly resolved in the MIKE 3 simulations, indicate the presence of mesoscale eddy-like circulation patterns. At the surface, seasonal-mean velocities range from 0.10 to 0.35 m s^{-1}, with maxima exceeding 0.40 m s^{-1} along the northwestern margin between the Strait of Hormuz and Sirik. The modeled inflow toward the Strait exhibits mean velocities of approximately 0.20–0.30 m s^{-1}, consistent with pressure-driven exchange associated with Persian Gulf Water (PGW) outflow. Comparison with HYCOM shows strong agreement, with spatial correlation exceeding $R = 0.75$, RMSE in the range of 0.05–0.08 m s^{-1}, and negligible mean bias ($< \sim 0.02$ m s^{-1}).

At 25 m depth, velocity magnitudes decrease slightly (0.08–0.28 m s^{-1}), while vertical shear intensifies due to the combined effects of Ekman dynamics and baroclinic pressure gradients. The cyclonic structure persists, although with reduced spatial coherence relative to the surface, reflecting the vertical modulation of eddy structures. Statistical comparison indicates robust agreement, with correlation coefficients in the range $R = 0.70$–0.75, RMSE values of approximately 0.06–0.09 m s^{-1}, and mean bias remaining within $\pm$ 0.03 m s^{-1}.

At 60 m depth, circulation reflects a predominantly baroclinic regime, with velocity magnitudes between 0.05 and 0.20 m s^{-1} and a persistent eastward undercurrent along the Omani coast. This feature represents the subsurface expression of PGW spreading into the Arabian Sea and is consistent with a two-layer exchange circulation. Model performance at this depth shows a moderate reduction in agreement, with spatial correlation around $R \approx 0.65$, RMSE values of 0.07–0.10 m s^{-1}, and mean bias generally within $\pm$ 0.03–0.04 m s^{-1}, reflecting increased sensitivity to stratification and vertical mixing parameterizations.

During the summer monsoon (Southwest monsoon), strong southwesterly winds (seasonal mean wind stress ~ 0.1–0.2 N m^{-2}) reverse the surface circulation and intensify coastal currents along the Omani margin, with velocities reaching 0.35–0.45 m s^{-1}. This intensification is associated with offshore Ekman transport and coastal upwelling, which enhance horizontal density gradients and strengthen alongshore jets. The MIKE 3 simulations capture these processes and reveal coherent circulation patterns that are consistent with mesoscale variability observed in the HYCOM dataset. Model–HYCOM comparison during summer shows consistent skill across all layers, with surface correlation remaining above $R = 0.70$, decreasing to approximately $R = 0.65$ at 25 m and $R \approx 0.60$ at 60 m. RMSE values increase slightly relative to winter but remain within 0.06–0.11 m s^{-1} across all depths, while mean bias remains small ($< \pm$ 0.04 m s^{-1}), indicating no systematic over- or underestimation.

Seasonal reversal of the horizontal gyre structure is primarily controlled by monsoon wind forcing, whereas tidal dynamics maintain a persistent barotropic background flow throughout the year. The relative contribution of baroclinic forcing increases with depth, particularly below 50 m, where density gradients associated with PGW outflow dominate the momentum balance. Overall, the fully forced simulation reproduces both the amplitude (within ~ 10–15% of HYCOM mean velocities) and the phase of seasonal circulation variability across all depth layers. Importantly, the results demonstrate that the MIKE 3 model is capable of resolving the principal mesoscale circulation features, including eddy-like structures, while maintaining strong agreement with the HYCOM reanalysis.

In Press

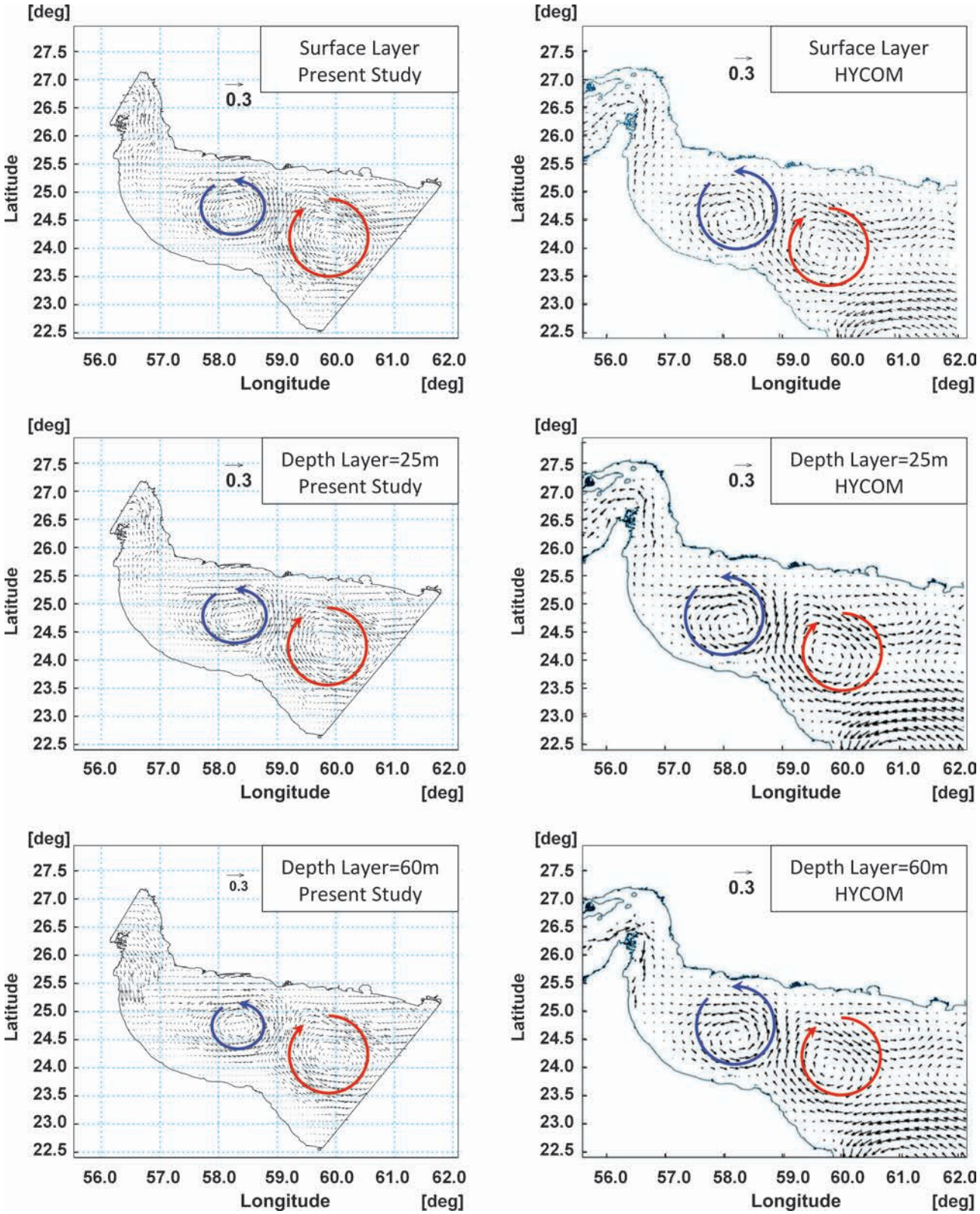


Figure 6. Spatial comparison of seasonal mean current velocity fields in the Gulf of Oman from the MIKE 3 model and the Global HYCOM reanalysis (2012) at the surface and at depths of 25 m and 60 m during the cold season. The results highlight coherent circulation patterns, including mesoscale eddy-like structures, captured by both datasets

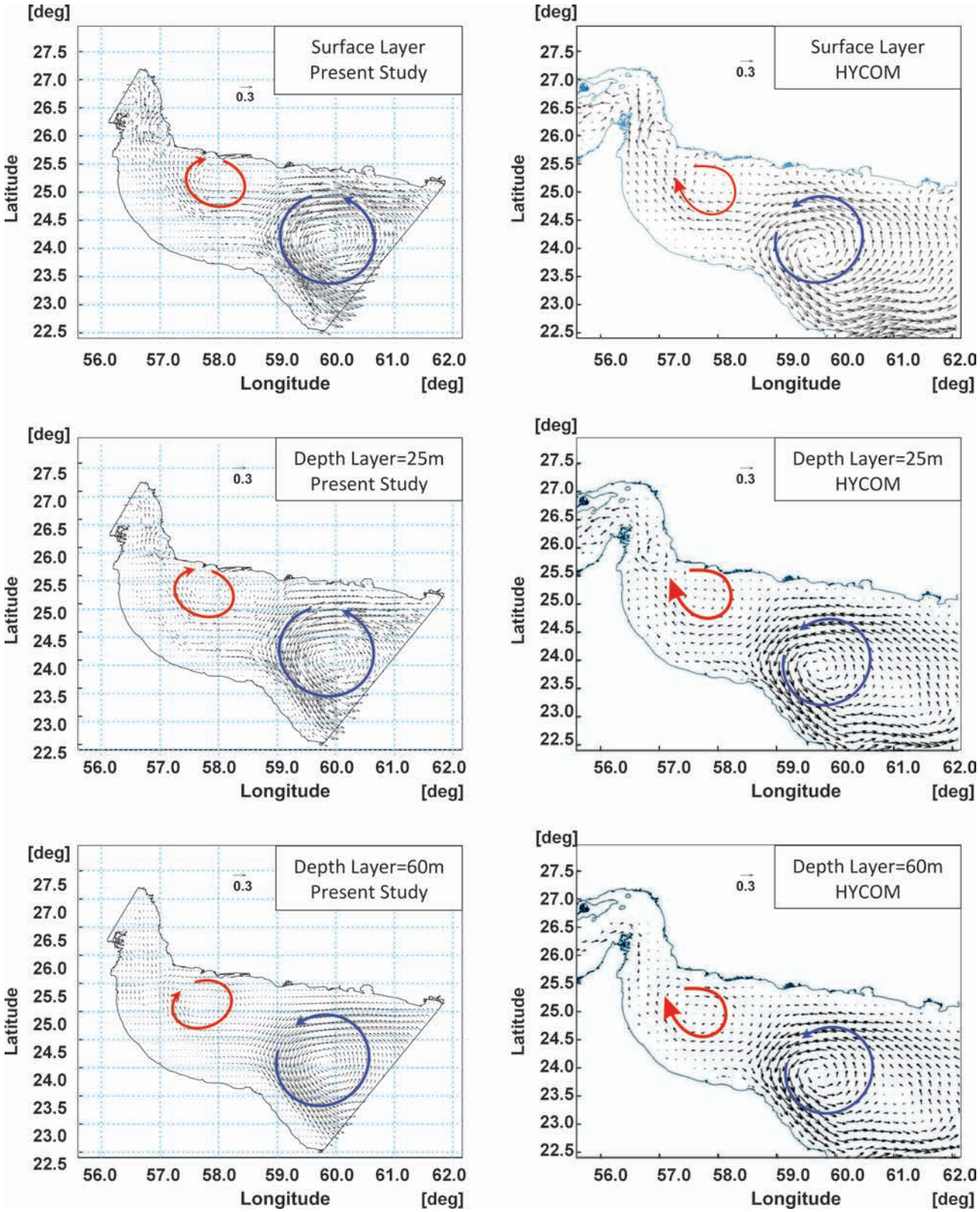


Figure 7. Spatial comparison of seasonal mean current velocity fields in the Gulf of Oman from the MIKE 3 model and the Global HYCOM reanalysis (2012) at the surface and at depths of 25 m and 60 m during the warm season. The simulated fields reveal consistent mesoscale eddy-like circulation features across different depth layers.

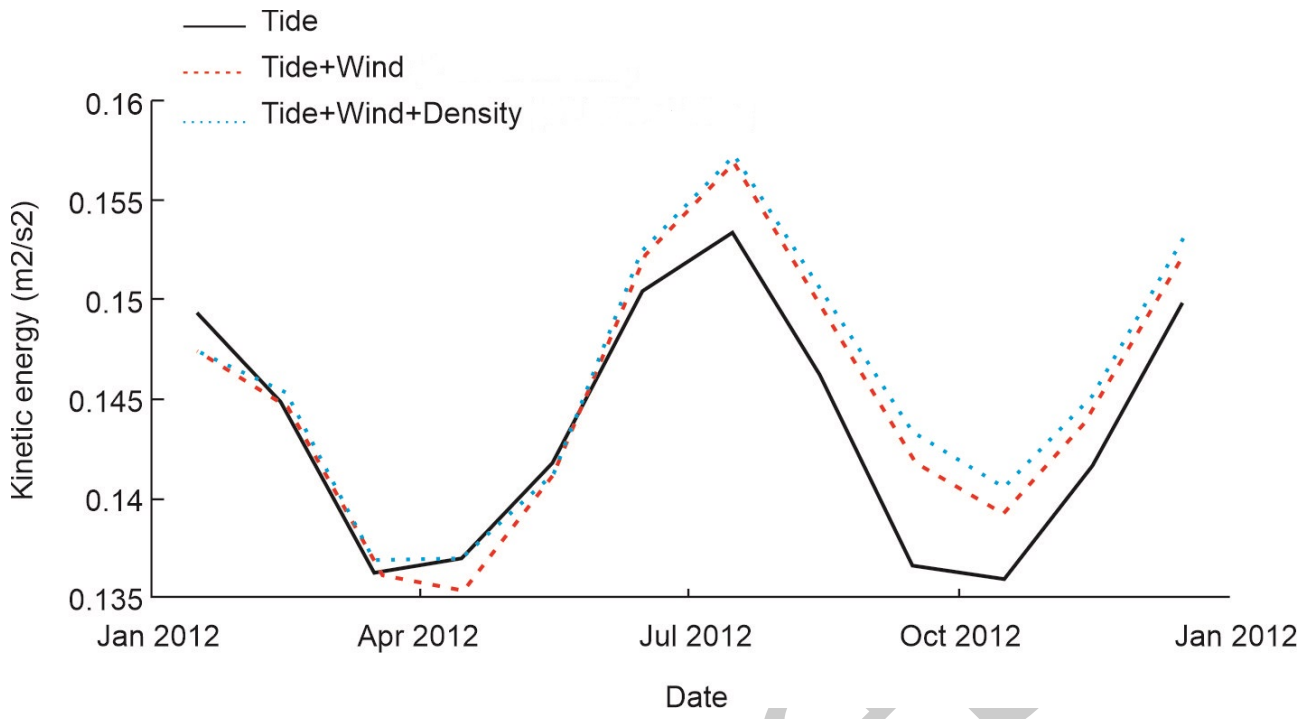


Figure 8. Monthly depth averaged kinetic energy at Station B calculated from simulation with forcing: tide (solid black), mixed tide and wind (red dashed line) and mixed tide, wind and density (blue dotted).

4.2 Kinetic energy decomposition

To quantitatively assess the relative contribution of different forcing mechanisms, depth-averaged kinetic energy (KE) was computed for each simulation scenario. The kinetic energy per unit mass was defined as:

$$KE = 12(u^2 + v^2) \tag{6}$$

where u and v are the horizontal velocity components. Monthly depth-averaged values were calculated to evaluate seasonal variability.

Figures 8 presents the temporal evolution of kinetic energy during 2012 for the tide-only, tide–wind, and tide–wind–density simulations.

The tide-only simulation produces a relatively stable kinetic energy signal throughout the year, with values ranging between 0.136 and 0.154 $m^2\ s^{-2}$. Biannual maxima occur during periods of intensified tidal forcing associated with seasonal modulation.

When wind forcing is incorporated, kinetic energy exhibits a seasonal response, particularly during the Southwest monsoon (July–September). Relative to the tide-only simulation, wind forcing increases depth-averaged kinetic energy by approximately 2.50%, with the strongest enhancement occurring during peak monsoon conditions. However, this difference was not statistically significant ($p = 0.10$; 95% CI: -0.01 to 0.05), indicating that the magnitude of the wind-related increase should be interpreted cautiously.

The inclusion of density-driven processes further modifies the kinetic energy distribution. In the fully forced simulation (tide–wind–density), kinetic energy increases by approximately 2.18% relative to the tide-only case. However, this difference was also not statistically significant ($p = 0.085$; 95% CI: -0.015 to 0.04). Therefore, the relatively small changes associated with wind and density forcing should not be interpreted as statistically distinct from the variability represented in the simulations.

Overall, the results indicate that tidal forcing establishes the primary energetic framework of the system, while wind and density-driven processes produce relatively small additional changes in basin-scale kinetic energy. Wind forcing shows the larger secondary contribution, particularly during the summer monsoon, whereas density-driven processes primarily influence subsurface structure and seasonal variability. Given the lack of statistical significance, these percentage differences are interpreted as indicative of relative energetic influence rather than robust quantitative changes.

5. Discussion

The staged modeling framework implemented in this study provides a quantitative decomposition of the relative contributions of tidal, wind-driven, and density-induced processes to circulation in the Gulf of Oman. Results indicate that tidal forcing forms the dominant energetic backbone of the system, while wind stress modulates seasonal vari-

In Pre

ability and density gradients primarily affect vertical structure. Wind and density processes were associated with increases in basin-scale kinetic energy of approximately 2.50% during the summer monsoon and 2.18% during winter conditions; however, these differences were not statistically significant, consistent with a secondary role for these forcing mechanisms.

The dominance of tidal forcing is closely linked to the basin geometry, particularly the constriction near the Strait of Hormuz, which enhances barotropic tidal currents and supports efficient energy propagation. This is consistent with previous studies (Reynolds, 1993; Pous et al., 2004), while the present work provides a quantitative separation of tidal, wind, and density contributions, highlighting the primarily tide-dominated nature of the system.

Wind forcing has its strongest impact during the Southwest monsoon, when persistent southwesterly winds reorganize surface circulation, intensify coastal currents, and enhance offshore Ekman transport and upwelling. Despite these dynamical effects, its contribution to depth-integrated kinetic energy remains limited, indicating a partial decoupling between surface wind forcing and basin-scale energetics compared to more wind-dominated regimes such as the northern Arabian Sea (Schott and McCreary Jr, 2001; Vinayachandran et al., 2013). This interpretation should be treated with caution, as depth- averaged kinetic energy in a strongly tide-dominated system is likely dominated by the tidal signal, which may mask the true magnitude of wind-driven variability. A more robust assessment of the coupling between wind forcing and circulation would require spectral or cross-spectral analysis to isolate the wind-band variance from the tidal signal, which was beyond the scope of the present study.

The relatively weak response of basin-scale depth-averaged kinetic energy to wind forcing should be interpreted cautiously, given the strongly tide-dominated nature of the system. The dominant tidal signal may mask wind-driven variability in depth-averaged kinetic energy; therefore, the observed response does not necessarily imply weak coupling between surface wind forcing and circulation. Spectral or cross-spectral analysis could provide a more robust assessment of this coupling and represents a useful direction for further strengthening the analysis.

Density-driven processes associated with Persian Gulf Water (PGW) primarily influence subsurface circulation and stratification but contribute only modestly to basin-scale kinetic energy. This is due to the spatial confinement of strong density gradients and the mitigating effect of tidal mixing, which reduces stratification over much of the basin. Consequently, baroclinic processes are more relevant for vertical structure and water mass transformation than for large-scale energy balance.

Model validation against HYCOM demonstrates robust performance across all depth layers. At the surface, high agreement is obtained ($R > 0.75$, RMSE ≈ 0.05–$0.08\ m\ s^{-1}$), while at 25 m and 60 m depth, correlation decreases slightly ($R \approx 0.70$–0.75 and $R \approx 0.65$, respectively), with increasing RMSE reflecting stronger stratification effects. This systematic reduction in skill with depth is physically consistent with the transition from barotropic to baroclinic dynamics, while overall agreement remains satisfactory across seasons and depths. It should be emphasized that this comparison against HYCOM does not constitute fully independent validation, since HYCOM is itself a numerical model and was also used to provide open boundary and initial conditions for the baroclinic simulation; agreement with HYCOM therefore reflects consistency between two model products rather than a direct comparison with independent observations, and should be interpreted accordingly alongside the in-situ RCM9 and tide-gauge validation presented in Section 3.

Although the inclusion of density-driven processes does not significantly improve statistical model performance metrics (e.g., RMSE and correlation), this does not imply a negligible physical role. Validation metrics are primarily controlled by dominant barotropic and wind-driven variability captured at limited observation points, whereas density-driven processes exert their influence mainly on vertical structure and basin-scale energetics, which are not fully resolved by point-based measurements.

Seasonal analysis shows that the model captures the monsoon-driven reversal of surface circulation and associated intensification of coastal currents, along with increased vertical shear during summer. Although agreement with HYCOM slightly decreases at depth during summer, the model still reproduces the main circulation patterns and seasonal variability.

Overall, circulation in the northern Gulf of Oman is primarily controlled by tidal forcing, with monsoonal winds providing seasonal modulation and density-driven processes refining vertical structure. This hierarchy of forcing mechanisms underscores the dominance of barotropic dynamics in the basin. The combined analysis of forcing decomposition and vertically consistent validation provides a robust framework for understanding shelf circulation and supports future applications in coastal dynamics and marine management.

Several limitations remain. The bathymetric resolution may not fully capture small-scale coastal features, while the ERA5 forcing (0.25°) may underestimate local wind variability. Uncertainties in mixing parameterizations and open boundary conditions also affect subsurface dynamics. Additionally, HYCOM itself contains inherent reanalysis uncertainties, which should be considered when interpreting validation metrics.

6. Conclusions

This study investigated the relative influence of tidal, wind-driven, and density-driven processes on circulation in the northern Gulf of Oman using a three-dimensional hydrody-

In Press

namic model and a forcing- based simulation framework. Model validation against observed water levels and current velocities demonstrated satisfactory agreement, supporting the use of the model for examining the dominant circulation processes.

The results show that tidal forcing provides the primary energetic control of the northern Gulf of Oman, establishing the dominant basin-scale circulation and kinetic energy. Wind forcing acts as the most important secondary mechanism, primarily enhancing seasonal surface circulation during the Southwest monsoon, whereas density-driven processes associated with Persian Gulf Water outflow exert a smaller energetic influence but play an important role in shaping subsurface and vertical circulation structure.

The relatively small changes in depth-averaged kinetic energy associated with wind and density forcing should be interpreted cautiously, as the dominant tidal signal may mask their influence at the basin scale. Thus, the results demonstrate that the energetic dominance of tides does not imply an absence of physically important wind- and density-driven processes, particularly in the surface and subsurface layers.

The main contribution of this study is the quantitative comparison of the relative energetic influence of major forcing mechanisms within a strongly tide-dominated, monsoon-influenced shelf system. This forcing-based framework provides a useful basis for interpreting circulation controls in the northern Gulf of Oman and may be transferable to other regions where tidal, atmospheric, and density-driven processes interact. The findings also provide a quantitative basis for prioritizing future observational and modeling efforts, particularly those aimed at resolving seasonal wind-driven variability and subsurface density-driven circulation.

Conflict of interest

None declared.

References

Deshpande, M., Singh, V. K., Ganadhi, M. K., Roxy, M. K., Emmanuel, R., Kumar, U., 2021. *Changing status of tropical cyclones over the north Indian Ocean*. Climate Dynam. 57(11), 3545–3567.

Ezam, M., Bidokhti, A. A., Javid, A. H., 2010. *Numerical simulations of spreading of the Persian Gulf outflow into the Oman Sea*. Ocean Sci. 6(4), 887–900.

Hersbach, H., Bell, B., Berrisford, P., Hirahara, S., Horányi, A., Muñoz-Sabater, J., Nicolas, J., Peubey, C., Radu, R., Schepers, D., 2020. *The ERA5 global reanalysis*. Quarter. J. Royal Meteorol. Soc. 146(730), 1999–2049.

Metzger, E. J., Smedstad, O. M., Carroll, S. N., 2009. *User's Manual for the Global Ocean Forecast System (GOFS)*, Ver. 3.0.

Reynolds, R. M., 1993. *Physical oceanography of the Gulf, Strait of Hormuz, and the Gulf of Oman – Results from the Mt Mitchell expedition*. Marine Pollut. Bull. 27(C), 35–59. https://doi.org/10.1016/0025-326X(93)90007-7

Padman, L., Erofeeva, S., 2005 *Tide model driver (TMD) manual*. Earth Space Res.

Pous, S. P., Carton, X., Lazure, P., 2004. *Hydrology and circulation in the Strait of Hormuz and the Gulf of Oman—Results from the GOGP99 Experiment: 1. Strait of Hormuz*. J. Geophys. Res.-Oceans 109(C12).

Resplandy, L., Lévy, M., Madec, G., Pous, S., Aumont, O., Kumar, D., 2011. *Contribution of mesoscale processes to nutrient budgets in the Arabian Sea*. J. Geophys. Res.-Oceans 116(C11).

Schott, F. A., McCreary Jr, J. P., 2001. *The monsoon circulation of the Indian Ocean*. Progress Oceanogr. 51(1), 1–123.

Simpson, J. H., Sharples, J., 2012. *Introduction to the physical and biological oceanography of shelf seas*. Cambridge Univ. Press.

Thoppil, P. G., Hogan, P. J., 2010. *Persian Gulf response to a wintertime shamal wind event*. Deep-Sea Res. Pt. I 57(8), 946–955.

Trott, C. B., Subrahmanyam, B., Murty, V. S. N., 2017. *Variability of the Somali Current and eddies during the southwest monsoon regimes*. Dynam. Atmos. Oceans 79, 43–55.

Vinayachandran, P. N., Shankar, D., Vernekar, S., Sandeep, K. K., Amol, P., Neema, C. P., Chatterjee, A., 2013. *A summer monsoon pump to keep the Bay of Bengal salty*. Geophys. Res. Lett. 40(9), 1777–1782.

Weatherall, P., Ferreras, S. C., Cardigos, S. D. A., Cornish, N., Davidson, S. R., Dorschel, B., Drennon, H., Ferrini, V., Harper, H. A., Isler, T., 2024. *The GEBCO_2024 Grid – a continuous terrain model of the global oceans and land*.

DHI, 2007. *User Guide for MIKE 3* (Estuarine and Coastal Hydraulics and Oceanography, Hydrodynamic Module). Sci. Document.

Wiggert, J. D., Hood, R. R., Banse, K., Kindle, J. C., 2005. *Monsoon-driven biogeochemical processes in the Arabian Sea*. Progr. Oceanogr. 65(2–4), 176–213.

Wu, J., 1980. *Wind-stress coefficients over sea surface near neutral conditions – A revisit*. J. Phys. Oceanogr. 10(5), 727–740.

Wu, J., 1994. *The sea surface is aerodynamically rough even under light winds*. Boundary-Layer Meteorol. 69(1), 149–158.

In Press